





# Raw Data Simulation Under Undulating Terrain for Bistatic SAR With Arbitrary Configuration

Wenchao Li , *Member, IEEE*, Lei Wang, Dan Liu, Tianfu Chen, *Student Member, IEEE*,  
Zhongyu Li , *Member, IEEE*, Junjie Wu , *Senior Member, IEEE*, Haiguang Yang, *Member, IEEE*,  
and Jianyu Yang , *Member, IEEE*

**Abstract**—Raw data simulation is very important for system parameter design, performance evaluation, and route planning of bistatic synthetic aperture radar (SAR). However, most conventional simulation methods focus on improving the efficiency of echo simulation, without considering the impact of terrain fluctuations, resulting in insufficient fidelity of simulated echoes. In this article, a raw data simulation framework under undulating terrain for bistatic SAR with arbitrary configuration is proposed. In the framework, based on the prior information of digital elevation model of undulating terrain and the small facet theory, the time-variant scattering coefficient is computed first with the empirical formula related with the angle variation of transmitter and receiver for bistatic SAR. Then the shadow is judged from the perspectives of transmitter and receiver, respectively, and the formation of double shadow is discussed. At last, the above process was embedded into the time domain pulse by the pulse echo simulation algorithm, forming a framework for simulating bistatic SAR raw data under undulating terrain with arbitrary configuration, and the simulated and measured data experiments are illustrated to verify the effectiveness of the proposed framework.

**Index Terms**—Bistatic synthetic aperture radar (SAR), double-shadow phenomenon, raw data simulation, SAR shadow simulation, undulating terrain.

## I. INTRODUCTION

UNDULATING terrain synthetic aperture radar (SAR) raw data simulation plays an important role in SAR system parameter design, SAR route planning, imaging algorithm verification, performance evaluation, and SAR image postprocessing [1], [2], [3]. Bistatic SAR, whose transmitter and receiver are mounted on different platforms, has more flexible configurations and more complex imaging processing than monostatic SAR [4], [5], [6], which means that raw data simulation for bistatic SAR is much more important.

As to the simulation of SAR raw data, most of the works focus on the simulation algorithms, and they can be classified as time domain algorithms [7], [8], [9], [10], [11] and frequency

domain algorithms [12], [13], [14], [15], [16]. These algorithms in different domains have different merits. Generally, the time domain algorithms can simulate raw data of SAR with arbitrary configuration and can effectively embed the impact of platform motion errors [17], [18], while the frequency domain algorithms have higher computational efficiency, but always with some configuration limitations [19].

The simulation algorithms mentioned above play an important role in the verification of imaging processing algorithms and the design of system parameters. However, the flat terrain assumption is often made in these simulations, and the influence of terrain is not considered, so the simulation results of raw data usually cannot reflect the special phenomena in SAR image, such as the shadow occlusion, which not only can reflect the accuracy of the simulated raw data but also can be used in many subsequent processing, such as moving target indication [20] and target height estimation [21], [22]. Hence, the raw data simulation of SAR considering undulating terrain is necessary, which also provides a foundation for the construction of deep network datasets [23], [24].

One key point for SAR raw data simulation considering undulating terrain is to acquire the scene scattering coefficient. In principle, it can be obtained through electromagnetic calculations [25], [26], which always takes a large amount of computation time. Therefore, such methods are mainly used for accurate modeling of typical targets with relatively small size, such as the building, the airplane, or other man-made targets. The other is based on scattering statistical models [27]. This kind of method usually divides the actual terrain into facet elements, and then obtains the scene scattering coefficient based on the empirical formula. For example, the monostatic SAR raw data simulation methods considering 3-D scene in [28], [29], and [30]. Besides, SAR echo simulation methods for specific scenarios, such as oceans and forests, have been developed in [31], [32], and [33]. However, they cannot be applied to bistatic SAR directly due to the differences in geometric configuration and scattering characteristics. Besides, many electromagnetic scattering analytical solutions, such as the small perturbation method [34], geometrical optics [35], physical optics [36], AIEM [37], small-slope approximation [38], and bistatic anisotropic polarimetric two-scale model [39] have been developed in recent years. Especially, the AIEM method has been widely used, and the simplified empirical statistical model based on AIEM has been developed in [40].

Manuscript received 22 March 2024; revised 25 May 2024 and 8 July 2024; accepted 9 July 2024. Date of publication 15 July 2024; date of current version 24 July 2024. This work was supported in part by the National Natural Science Foundation of China under Grant 62171107 and in part by the Sichuan Provincial Natural Science Foundation General Project under Grant 2024NSFSC0481. (Corresponding author: Wenchao Li.)

The authors are with the School of Information and Communication Engineering, University of Electronic Science and Technology of China, Chengdu 611731, China (e-mail: lwc6@163.com).

Digital Object Identifier 10.1109/JSTARS.2024.3427704

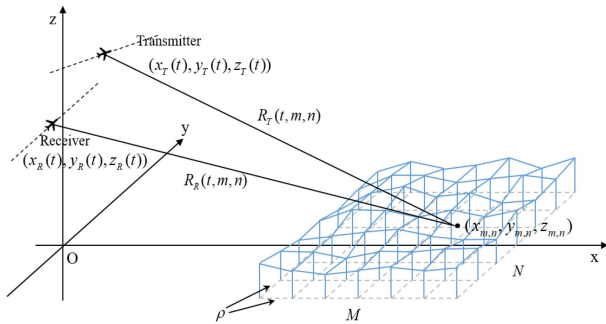


Fig. 1. Bistatic SAR geometry model with undulating terrain.

Another key point for SAR raw data simulation considering undulating terrain is the judgment of shadow area. At present, it mainly can be divided into the ray tracing method [41] and angle comparison method [42]. The former method follows the geometrical optics model, imitating the propagation process of light in space, and can effectively handle multiple scattering, shadowing and occlusion effects. However, this method needs to trace the path of a large number of rays, resulting in a huge amount of calculation. As the imaging scene increases, the computational efficiency of the algorithm will drop rapidly.

On the contrary, the latter method utilizes the different viewing angles of the radar to each target point to judge the occlusion situation, which can effectively simulate the SAR shadow of the undulating terrain. But it always faces the problem of insufficient accuracy. For example, by comparing the elevation angle of each grid on the same line of sight, an elevation-angle-based shadow judging method is proposed in [43] and [44]. This method is easy to implement and can be used to quickly judge shadows. However, it is based on the assumption that the radar beam is a plane wave and the effect of beamwidth is not considered, which would lead to inaccurate shadow judgment results in the elevation-angle-based method. With the assumption of spherical wave, the method in [29] divides the radar beam into two dimensions, and then judge shadows in each azimuth beam grid. But it cannot guarantee that the targets in the same beam grid are on the same line of sight, which leads to many targets unable to be judged. A dynamic elevation angle interpolation (DEAI) algorithm for SAR shadow simulation is proposed in [42], but multiple interpolations will introduce error accumulation, and the shadow of the undulating terrain contour may be smoothed to a certain extent, resulting in an inaccurate shadow judgment.

In addition to the common issues mentioned above, there are also some new features for the raw data simulation of bistatic SAR. For example, the scattering features are different due to the separation of transmitter and receiver, hence the empirical scattering coefficient equation should be modified accordingly. Meanwhile, the shadow occlusion is different, and we should evaluate the occlusion both from the perspectives of transmitter and the receiver, and there may be double shadows in bistatic SAR image. Besides, how to evaluate the effectiveness of the simulation scheme is another problem. In this article, a simulation framework for raw data of bistatic SAR under undulating terrain is proposed. In the framework, based on the prior information of digital elevation model (DEM) and the

small facet fitting method, the time-variant scattering coefficient is computed first with the empirical formula related with the angle variation of transmitter and receiver, and the shadow is judged by the elevation angle comparison from the perspectives of transmitter and the receiver, respectively. Meanwhile, the double shadow phenomena are analyzed and its formation condition is discussed. At last, the simulation framework of raw data for bistatic SAR under undulating terrain is formulated combined with the pulse-by-pulse simulation algorithm, and the simulated and measured data experiments are presented. Besides, the comparisons between the proposed scheme and the benchmark obtained by the ray tracing shadow judgment and time-domain pulse-by-pulse simulation algorithm are made to further illustrate the effectiveness of the proposed framework.

Moreover, since the geometry of bistatic SAR can be divided into two types: 1) translational invariant and 2) translational variant. In translational invariant bistatic SAR, the transmitter and receiver move with the same velocities, while they move with different velocities in translational variant bistatic SAR [45], [46]. In this article, the two sets of simulation experiments belong to the above two modes have been illustrated to validate the effectiveness of the proposed method, which means that it is suitable for bistatic SAR with arbitrary configuration. In addition, different imaging algorithms of bistatic SAR, such as range Doppler [47], chirp scaling [48],  $\omega$ - $k$  [49], and back projection (BP) [50] algorithms can be adopted to validate the effectiveness of the simulated raw data. Considering that the frequency domain imaging algorithms usually have the restrictions of geometry configuration, the time domain BP algorithm, which can be applied to arbitrary bistatic configurations, is used in this article.

The main contribution of this article is summarized as follows. First, a raw data simulation framework under undulating terrain for bistatic SAR with arbitrary configuration is developed, which mainly includes the time-varying scattering coefficient computation by the empirical formula related with the angle variation of transmitter and receiver, and the shadow judgment by the elevation angle comparison from the perspectives of transmitter and the receiver, respectively. Second, the double shadow phenomena of bistatic SAR are analyzed and its formation condition is discussed. At last, with the ray tracing shadow judgment method and pulse-by-pulse simulation algorithm as a benchmark, the effectiveness and efficiency of the proposed scheme has been illustrated.

The rest of this article is organized as follows. In Section II, the signal model of bistatic SAR will be illustrated. The acquisition process for scattering coefficients of undulating terrain and the shadow judgment method are given in Section III. The bistatic SAR raw data simulation framework will be shown in Section IV. The simulated and measured data experiments will be shown in Section V. Finally, Section VI concludes this article.

## II. RAW SIGNAL GENERATION FOR BISTATIC SAR

In this section, bistatic SAR raw signal model and the echo calculation equation will be established first according to the geometry configuration, and then the efficient simulation algorithm

in time domain will be illustrated, which lays the theoretical foundation for the subsequent simulation experiments.

The geometry configuration of bistatic SAR is shown in Fig. 1, where the transmitter and receiver fly along different trajectories, and their coordinates are  $(x_T(t), y_T(t), z_T(t))$  and  $(x_R(t), y_R(t), z_R(t))$ , respectively, where  $t$  is the azimuth slow time. The simulated undulating terrain scene can be approximated by many small facet cells with a grid of size  $M \times N$  and spacing  $\rho$  between adjacent grids. At a certain azimuth moment, the distance traveled by the radar wave incident from the transmitter to the facet cell grid  $(m, n)$  at coordinate  $(x_{m,n}, y_{m,n}, z_{m,n})$  in the scene and scattered back to the receiver is shown in (1) shown at the bottom of this page.

Assume that transmitted signal is a linear frequency modulated (LFM) pulse

$$s_t(\tau) = \text{rect}\left(\frac{\tau}{T_p}\right) \cdot \exp(j2\pi f_c \tau + j\pi K_r \tau^2) \quad (2)$$

where  $\tau$  denotes the fast time,  $K_r$  is the chirp rate,  $\text{rect}(\cdot)$  is the rectangular window function,  $T_p$  is the pulsewidth, and  $f_c$  is the carrier frequency. The time delay generated by the radar signal incident from the transmitter to the target and then scattered by the target back to the receiver is

$$t_d = \frac{R(t, m, n)}{c} = \frac{R_T(t, m, n) + R_R(t, m, n)}{c} \quad (3)$$

where  $c$  is the speed of light. Thus, the baseband echo signal can be expressed as

$$s(\tau, t; m, n) = \sigma(t; m, n) \cdot \text{rect}\left(\frac{\tau - t_d}{T_p}\right) \cdot \exp\left[-j2\pi f_c t_d + j\pi K_r (\tau - t_d)^2\right] \quad (4)$$

where  $\sigma(t; m, n)$  is the scattering coefficient of the grid  $(m, n)$ . The scattering coefficient of the whole undulating scene can be obtained by superimposing the scattering coefficients of all small facet cells, so the bistatic SAR echo signal of the undulating scene can be represented as

$$s(\tau, t) = \sum_{m=1}^M \sum_{n=1}^N \sigma(t; m, n) \cdot \text{rect}\left(\frac{\tau - R(t, m, n)/c}{T_p}\right) \cdot \exp\left[-j2\pi f_c R(t, m, n)/c + j\pi K_r (\tau - R(t, m, n)/c)^2\right] \quad (5)$$

Considering that the scattering coefficients and the shadow of SAR is time-varying and the configuration limitations of echo

simulation algorithms, the existing frequency-domain simulation method maybe invalid. Therefore, the time-domain pulse-by-pulse approach is used to generate echo data.

### III. CALCULATION OF SCATTERING COEFFICIENT AND SHADOW JUDGMENT

According to the echo calculation formula in Section II, the scattering coefficient calculation is a key step in SAR raw data simulation, which reflects the characteristics of the actual undulating terrain, and will be affected by the shadow occlusion. Besides, it varies with the change of the platform position at different azimuth moments, and this changing characteristic needs to be considered in order to achieve more accurate simulation.

In this section, the calculation method of bistatic SAR time-varying scattering coefficient for undulating terrain scenes will be presented first, and then an accurate shadowing judgment method is illustrated to determine the shadow of the transmitting and receiving stations, respectively. Finally, the conditions for the formation of the possible double-shadowing phenomenon of bistatic SAR are discussed.

#### A. Calculation of Time-Varying Scattering Coefficients

The small facet cell model is commonly used to calculate the scattering characteristics of the ground scene [28], where small facet cells are used to approximate a rough terrain surface, and each small facet cell is tangent to the actual plane, and the scattering characteristics of the ground scene are the result of coherent superposition of the scattered fields of all small facet cells.

Generally, the scattering characteristics of the actual ground scene are related to the scatterer shape, ground roughness, incidence angle of the radar wave, wavelength, and other factors. To facilitate the simulation, an empirical statistical model based on bistatic radar electromagnetic scattering [40], as shown in (6) shown at the bottom of the next page, is used to obtain the scattering coefficients, where  $\sigma$  represents the scattering coefficients,  $\theta_t$  and  $\theta_r$  are the local incident angles of the transmitter and receiver,  $\varphi_t$  and  $\varphi_r$  are the incident azimuth angles of the transmitter and receiver, respectively.  $P_1 \sim P_7$  are constants related to terrain type, carrier frequency, polarization mode, and their values under the terrain used in this article are shown in Table I. The frequency used in this article is X-band and the polarization mode is HH.

The small facet cell model adopts multiple adjacent data points of the DEM to fit a small facet cell tangential to the ground surface, and then find the parameters of the small facet cell. As

$$\begin{aligned} R(t, m, n) &= R_T(t, m, n) + R_R(t, m, n) \\ &= \sqrt{(x_T(t) - x_{m,n})^2 + (y_T(t) - y_{m,n})^2 + (z_T(t) - z_{m,n})^2} \\ &\quad + \sqrt{(x_R(t) - x_{m,n})^2 + (y_R(t) - y_{m,n})^2 + (z_R(t) - z_{m,n})^2} \\ &\text{where } 1 \leq m \leq M, 1 \leq n \leq N. \end{aligned} \quad (1)$$

TABLE I  
VALUES OF  $P_1 \sim P_7$

F	POL	$P_1$	$P_2$	$P_3$	$P_4$	$P_5$	$P_6$	$P_7$
L	HH	9.45	0.0017	1.43	-0.0003	1.6	84.05	1.53
	VV	25.90	0.107	2.178	1.232	1.98	189.14	1.52
S	HH	8.64	0.30	2.0	-0.009	0.11	46.13	1.21
	VV	88.15	-0.268	1.94	1.11	0.88	152.3	1.50
X	HH	2.2	0.33	1.8	-0.0075	0.098	27.60	0.90
	VV	46.18	-0.66	1.51	1.25	3.62	100.9	1.43
Ku	HH	4.39	0.30	1.80	-0.01	0.152	57.66	0.66
	VV	39.88	-0.0013	1.83	1.07	1.25	211.48	0.98

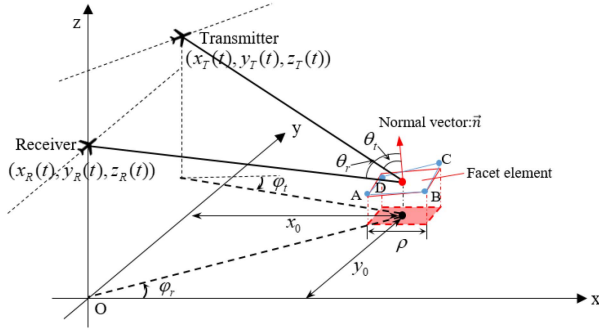


Fig. 2. Small facet cell model of undulating terrain.

shown in Fig. 2, supposing that the size of facet projected onto the ground is  $\rho$ , and the facet of a certain area is composed of four adjacent points  $A(x_1, y_1, z_1)$ ,  $B(x_2, y_2, z_2)$ ,  $C(x_3, y_3, z_3)$ , and  $D(x_4, y_4, z_4)$ . Hence, the plane equation fitted by these four points can be expressed as:  $z = a \cdot x + b \cdot y + c$ , and we can get the objective function

$$f = \sum_{i=1}^4 (z_i - (ax_i + by_i + c))^2. \quad (7)$$

Let  $\frac{\partial f}{\partial a} = \frac{\partial f}{\partial b} = \frac{\partial f}{\partial c} = 0$ , the coefficients  $a$ ,  $b$ , and  $c$  can be obtained, and then the coordinates of the center of the facet will be known:  $x_0 = (x_1 + x_3)/2$ ,  $y_0 = (y_1 + y_3)/2$ ,  $z_0 = a \cdot x_0 + b \cdot y_0 + c$

The incident beam vector of the transmitter to the small facet cell is  $(x_0 - x_T(t), y_0 - y_T(t), z_0 - z_T(t))$ , and then the incident wave vector and the normal vector of the small facet cell are dotted to obtain the local incidence angle as (8) shown at the bottom of this page. Similarly, the scattered beam vector of the receiver to the small facet cell is  $(x_R(t) - x_0, y_R(t) - y_0, z_R(t) - z_0)$

$y_0, z_R(t) - z_0$ ), and the local scattering angle can be obtained as (9) shown at the bottom of this page. Besides, the incident azimuth angles of the transmitter and receiver can be calculated as (10) and (11), respectively

$$\varphi_t = \tan^{-1} [(y_0 - y_T(t)) / (x_0 - x_T(t))] \quad (10)$$

$$\varphi_r = \tan^{-1} [(y_0 - y_R(t)) / (x_0 - x_R(t))]. \quad (11)$$

In addition, the choice of facet size is usually a compromise between simulation accuracy and computational efficiency. Generally, the smaller the facet, the higher the accuracy of echo simulation, and the greater the computational burden. Besides, the facet size is usually smaller than the resolution cell determined by SAR system parameters, but larger than incident wavelength [1]. Besides, the intensity of speckle mainly depends on the size of the facet relative to the resolution cell. Generally speaking, the smaller the facet relative to the resolution cell, the more obvious the speckle noise, and vice versa, which would be validated in the part of simulations.

Besides, because SAR echo simulation of different scenarios often have different characteristics. For example, the raw data simulation of ocean scenes often requires consideration of the Bragg effect [32], while the simulation of urban scenes often require consideration of multiple scattering [51]. Considering that bistatic SAR raw data simulation under undulating terrain is discussed in this article, the proposed method focuses on bistatic SAR shadow introduced by large-scale undulating terrain, and the primary scattering is mainly considered.

### B. Shadowing Judgment Method

Shadow judgment is a key part of the simulation of raw data for undulating terrain, which will directly determine the simulation accuracy. The traditional angle-based shadowing judgment method does not consider the influence of beam width and radar platform motion, resulting in a certain error in the judgment result. Therefore, in order to ensure the accuracy of shadow judgment in the simulation process and make the results more consistent with the actual SAR images, a shadow simulation scheme for SAR images of undulating terrain based on facet cell fitting and elevation angle comparison [52] is adopted here and compared with the ray-tracing method.

1) *Shadow Judgment With Elevation Angle Comparison*: For the bistatic SAR configuration, the transmitter and receiver are mounted on different platforms, and both will form shadows

$$\sigma = 10 \left[ \frac{P_1 \cos^{P_2} \theta_r \cos^{P_3} \theta_t (P_4 \sin \theta_t \sin \theta_r - \cos(\varphi_r - \varphi_t))^2}{(P_5 + P_6 \times (\sin^2 \theta_r + \sin^2 \theta_t - 2 \sin \theta_t \sin \theta_r \cos(\varphi_r - \varphi_t)))^{P_7}} \right]. \quad (6)$$

$$\theta_t = \cos^{-1} \left( \frac{|a \cdot (x_0 - x_T(t)) + b \cdot (y_0 - y_T(t)) - (z_0 - z_T(t))|}{\sqrt{a^2 + b^2 + 1} \cdot \sqrt{(x_0 - x_T(t))^2 + (y_0 - y_T(t))^2 + (z_0 - z_T(t))^2}} \right) \quad (8)$$

$$\theta_r = \cos^{-1} \left( \frac{|a \cdot (x_R(t) - x_0) + b \cdot (y_R(t) - y_0) - (z_R(t) - z_0)|}{\sqrt{a^2 + b^2 + 1} \cdot \sqrt{(x_R(t) - x_0)^2 + (y_R(t) - y_0)^2 + (z_R(t) - z_0)^2}} \right). \quad (9)$$

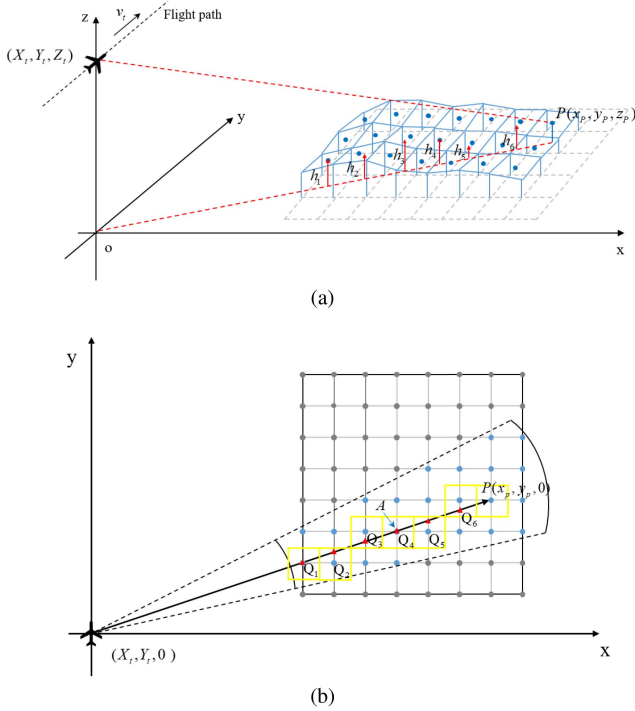


Fig. 3. Schematic of the proposed method in this article. (a) 3-D Schematic. (b) Top view schematic.

when imaging the undulating terrain area, so it is necessary to make shadow judgments separately during the simulation. Since judgment process is the same for the transmitter and receiver, here the transmitter is taken as an example to illustrate the judgment process of shadow. Based on the small facet cell fitting above, the irradiation range of the radar beam needs to be determined first

$$\text{Area}(\alpha, \phi) = \text{rect}\left(\frac{\alpha - \alpha_{\text{sq}}}{\alpha_{\text{azi}}}\right) \cdot \text{rect}\left(\frac{\phi - \phi_{\text{ld}}}{\phi_{\text{ele}}}\right) \quad (12)$$

where  $\text{rect}(\cdot)$  is a rectangular window function,  $\alpha_{\text{sq}}$  and  $\phi_{\text{ld}}$  represent the squint and elevation angles of the beam center, respectively.  $\alpha_{\text{azi}}$  and  $\phi_{\text{ele}}$  denote the beamwidth in azimuth and elevation directions, respectively.  $\alpha$  and  $\phi$  are the squint and elevation angles for the center of the facet, respectively, and they can be written as follows:

$$\alpha = \sin^{-1}\left(\frac{y_0 - y_T(t)}{R_T(t)}\right) \quad (13)$$

$$\phi = \sin^{-1}\left(\frac{z_T(t) - z_0}{R_T(t)}\right) \quad (14)$$

where  $\sin^{-1}(\cdot)$  is the arc sine function, and  $R_T(t)$  is the slant range from the center of the facet cell to the SAR.

The next step is to judge the occlusion of the grid points within the beam range. As shown in Fig. 3(a), the blues dots represent the center point of each fitted facet. Assuming that there are  $N$  facet cells  $Q_j (j = 1, 2, 3, \dots, N)$  on the beam line-of-sight path for the target point  $P(x_p, y_p, z_p)$ , and the corresponding fitted facet equation coefficient are  $a_j, b_j, c_j$ . Then, we can obtain the

height of each facet cell on the beam line-of-sight path for the target point P, as shown in the red dot in Fig. 3(a), respectively

$$h_j = a_j \cdot x_j + b_j \cdot y_j + c_j \quad (15)$$

where  $x_j$  is the coordinate of the center of the facet element on the X-axis,  $x_j = x_p - (N - j + 1) \cdot \rho$ , and the corresponding coordinates on the Y-axis is  $y_j = k \cdot x_j + Y_t$ , where  $k$  is the slope of the projection of the beam line of sight on the ground in Fig. 3(b)

$$k = \frac{y_p - y_T(t)}{x_p - x_T(t)}. \quad (16)$$

Hence, the corresponding elevation angle for the  $j$ th facet cell can be computed

$$\phi_j = \sin^{-1}\left(\frac{z_T(t) - h_j}{R_j}\right) \quad (17)$$

where  $R_j = \sqrt{(x_j - x_T(t))^2 + (y_j - y_T(t))^2 + (h_j - z_T(t))^2}$ . Similarly, the elevation angle  $\phi_p$  of target point P can be obtained. If there is a  $\phi_j$  which satisfies  $\phi_j < \phi_p$ , the target point P is considered to be occluded, and if all  $\phi_j$  have  $\phi_j \geq \phi_p$ , the target point P can be illuminated by the radar beam. In the beam range of the current azimuth moment, the occlusion judgment operation is performed on all grid points, and the shadow judgment result of the scene at the current moment can be obtained. According to the process above, we can see that the result of shadowing judgment also changes with the azimuth time, and the shading situation of the same target at different moments is different. Besides, the shadow occlusion of the receiver can be judged similarly.

In order to superimpose the shadow judgment result into the echo data, the general practice is to calculate the echo data of all grids in the scene first, and then perform the Hadamard product of the shadow function and the echo data. However, this approach generates many redundant computations, which leads to inefficient computation. Here, the shadow judgment results is superimposed on the scene scattering coefficients

$$\sigma_{mn}(t) = \sigma(t; m, n) \cdot \text{shadow}_T(t; m, n) \cdot \text{shadow}_R(t; m, n) \quad (18)$$

where  $\text{shadow}_T(t; m, n)$  and  $\text{shadow}_R(t; m, n)$  represent the judgment results of transmitting beam occlusion and receiving beam occlusion, respectively. When target grid  $(m, n)$  can be illuminated by the transmitter,  $\text{shadow}_T(m, n)=1$ , otherwise  $\text{shadow}_T(m, n)=0$ . Similarly, when the grid  $(m, n)$  can be illuminated by the receiver,  $\text{shadow}_R(m, n)=1$ , otherwise  $\text{shadow}_R(m, n)=0$ .  $\sigma_{mn}(t)$  represents the scattering coefficient of the grid after shadow superposition, and it can be written as follows:

$$\sigma_{mn}(t) = \begin{cases} \sigma(t; m, n), & \text{visible} \\ 0, & \text{invisible} \end{cases} \quad (19)$$

where visible means that the grid can be illuminated by both the transmitter and receiver, and invisible means at least one of the transmitter and receiver cannot illuminate the target grid.

Since the scene grids do not contribute to the echo data after being occluded by shadows, they can be ignored in the

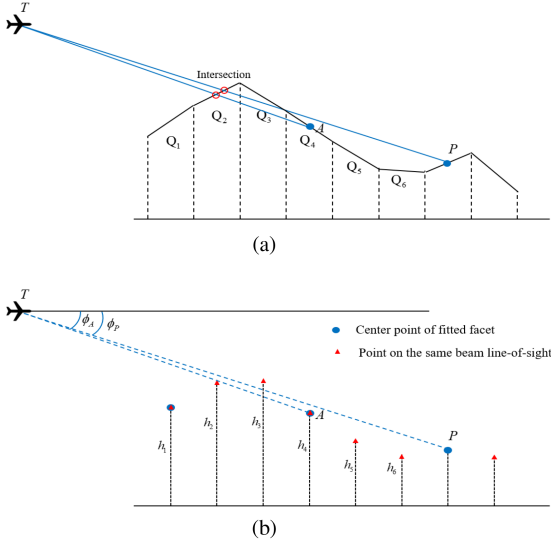


Fig. 4. Schematic of the shadow judgment method. (a) Ray tracing method. (b) Elevation angle comparison method.

calculation of echoes, which can greatly reduce the burden of echo calculation. Thus the echo calculation (5) can be modified as

$$s(\tau, t) = \sum_{m=1}^M \sum_{n=1}^N \sigma_{mn}(t) \cdot \text{rect} \left( \frac{\tau - R(t, m, n)/c}{T_p} \right) \cdot \exp \left[ -j2\pi f_c R(t, m, n)/c + j\pi K_r (\tau - R(t, m, n)/c)^2 \right]. \quad (20)$$

2) *Comparisons With Ray-Tracing Method:* In this part, the proposed method will be compared with the ray tracing method and the reasons for the efficiency improvement of the proposed method will be explained. Taking the facets where  $P$  is located in Fig. 3 as an example, the schematic diagrams of the ray tracing method and the elevation angle comparison method are shown in Fig. 4.

In the ray tracing method, we determine whether the ray pass through other facets during propagation based on the ray equation. Taking point  $A$  as an example, if the ray  $TA$  intersects with facets  $Q_1 \sim Q_3$ , it is considered that the target facet is occluded, otherwise the target can be illuminated. However, when judging the shadow of point  $P$ , due to different ray equations, ray  $TP$  must revisit the same facet  $Q_1 \sim Q_3$ , which means that it will be time-consuming [53].

The proposed method determines shadows by comparing the elevation angles of different facets on the same beam line-of-sight path. When judging the shadow of point  $A$ , the elevation angles  $\phi_i (i = 1 \sim 4)$  of facet  $Q_1 \sim Q_4$  have been calculated, and the minimum elevation angle  $\min(\phi_i (i = 1 \sim 4))$  has been obtained. According to Fig. 3, the grid points  $P$  and  $A$  are on the same beam line-of-sight path, hence, when judging the shadow of  $P$ , it is only necessary to compare the  $\phi_P$ ,  $\min(\phi_i (i = 1 \sim 4))$ , and  $\phi_i (i = 5, 6)$ . Besides, when there is little change in the azimuth beam line of sight, more points can be approximated

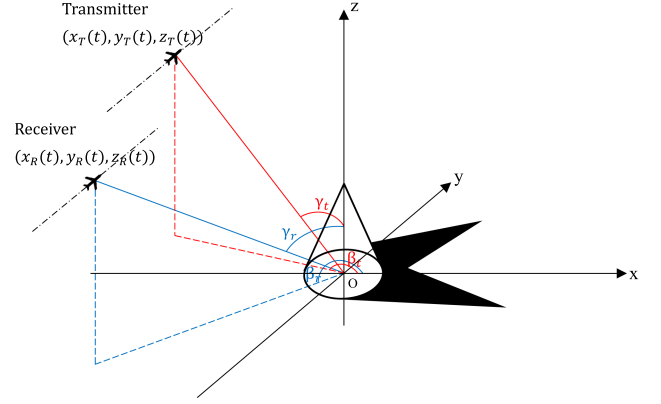


Fig. 5. Schematic diagram of bistatic SAR shadow.

with the center of the corresponding facets, which means that the proposed method can avoid multiple revisits to obtain shadow judgment results.

### C. Conditions for the Formation of Double Shadow

In practice, whether the imaging results exhibit double shadows depends on various factors, such as the bistatic SAR configuration, the shape of the target, and the difference in gain between the transmitting and receiving antennas. Here, the formation conditions of double shadows are discussed from the perspective of bistatic SAR configuration.

Generally, the direction and size of shadow should be considered. The direction of the shadow depends on the position of the light source when it illuminates the object, because the light propagates along a straight line, and the direction of the shadow of the object can be known by connecting the light source to the object and extending the line to the ground. The size of the shadow is not only related to the size of the object itself, but also with the location of the light source. Therefore, when judging the SAR shadow of undulating terrain, a coordinate system with the center of the scene as the origin is established first, as shown in Fig. 5, and the superposition of two shadows is determined by the position relationship between transmitter and receiver.

According to Fig. 5, the direction of the shadow is mainly determined by the angle between the aircraft and the scene. For the purpose of analysis and interpretation, the Cartesian coordinate system is first converted into a spherical coordinate system, and the respective conversion relationships of the transmitter and receiver in the two coordinate systems are

$$\begin{cases} R_t = \sqrt{x_T^2 + y_T^2 + z_T^2} \\ \beta_t = \tan^{-1} \left( \frac{y_T}{x_T} \right) \\ \gamma_t = \cos^{-1} \left( \frac{z_T}{R_t} \right) \end{cases} \quad (21)$$

$$\begin{cases} R_r = \sqrt{x_R^2 + y_R^2 + z_R^2} \\ \beta_r = \tan^{-1} \left( \frac{y_R}{x_R} \right) \\ \gamma_r = \cos^{-1} \left( \frac{z_R}{R_r} \right) \end{cases} \quad (22)$$

where  $R_t$  and  $R_r$  are the ranges of the transmitter and receiver to the origin,  $\beta_t$  and  $\gamma_t$  denote the azimuth and elevation angles of the transmitter,  $\beta_r$  and  $\gamma_r$  denote the azimuth and elevation

angles of the receiver, respectively. It can be seen that the directions of the shadows of the SAR transmitter and receiver are related to the azimuth angles  $\beta_t$  and  $\beta_r$ , and the shadow sizes depend on the elevation angles  $\gamma_t$  and  $\gamma_r$ . Accordingly, the shadow feature of the bistatic SAR system is further discussed as follows.

1)  $\beta_t = \beta_r$ : Since the direction of the shadow is determined by the azimuth angle, when the azimuth angles of the transmitter and receiver are equal, the shadows produced by them will overlap and superimpose along the same direction, and the superimposed relationship depends on the size of the elevation angle. When  $\gamma_t > \gamma_r$ , the transmitter's shadow is larger than the receiver's shadow, and the receiver's shadow will be covered by the transmitter's shadow; when  $\gamma_t < \gamma_r$ , the receiver's shadow will cover the transmitter's shadow; and when  $\gamma_t = \gamma_r$ , the two shadows are exactly the same. Therefore, there is only one shadow on the final imaging result, and double-shadow phenomenon will not occur.

2)  $\beta_t \neq \beta_r$ : When the azimuth angles are not equal, the relationship between the transmitter shadow and the receiver shadow is more complex. For simplicity, the variation of the double-shadow phenomenon can be determined by comparing the size of the area of the two shadows and determining whether one of the shadows is completely covered by the other shadow. If the transmitter shadow is larger than the receiver shadow, we will go to determine whether all the receiver shadow pixel points belong to the transmitter shadow. If each point can find a corresponding location, the receiver shadow is considered to be completely covered by the transmitter shadow, and only the transmitter shadow will be present in the imaging result. Conversely, if the transmitter shadow is smaller, then this method can also be used to determine whether the transmitter shadow is completely covered. As long as one shadow cannot be completely covered by the other shadow, it is considered that double-shadow phenomenon will appear. All the analysis will be validated via the simulation results in Section V.

#### IV. BISTATIC SAR RAW DATA SIMULATION FRAMEWORK

According to the scattering coefficient calculation and shadowing judgment methods proposed in Section III, combined with the time domain pulse by pulse echo simulation algorithm in Section II, bistatic SAR raw data simulation framework for undulating terrain is formulated in this section, just as shown in Fig. 6, and the detailed implementation steps are as follows.

- 1) Set the simulation parameters and geometric configuration of the bistatic SAR and input the DEM data of the scene.
- 2) Fit the small surface cells using the DEM data of the scene to obtain the coordinates of the center position of the small facet cells and the plane normal vectors.
- 3) Calculate the angle of incidence, angle of scattering, and elevation angle of view of the radar transmitting and receiving beams for small facet cells at current azimuth time.
- 4) Calculate the scattering coefficient of the small facet cell according to (6).

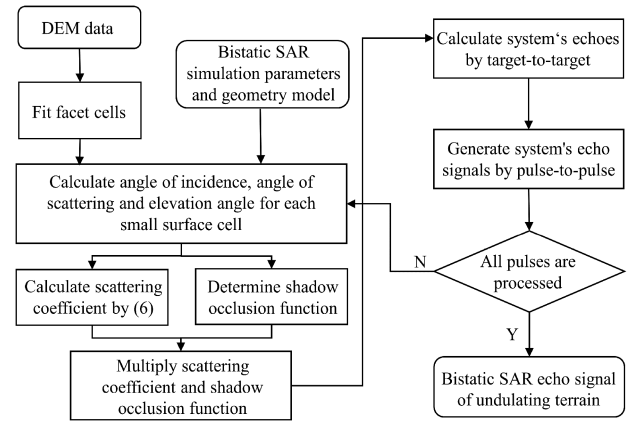


Fig. 6. Flow chart of the proposed scheme.

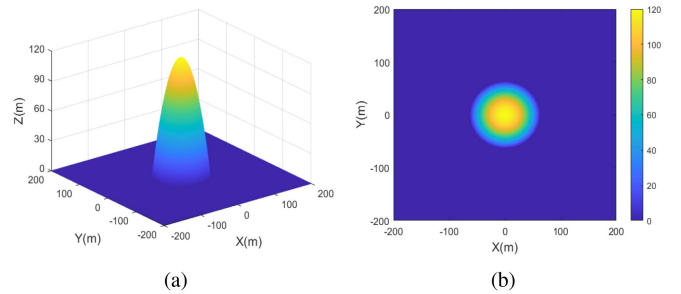


Fig. 7. Digital elevation data for simulated ideal undulating terrain. (a) 3-D terrain. (b) 2-D top view of (a).

- 5) Determine the shadow occlusion function of small facet cells using the proposed method.
- 6) Multiply the results of (d) and (e) to obtain the scattering coefficient of the scene at the current time.
- 7) Calculate system's echoes by target to target with (20) given a slow time instant.
- 8) Generate system's echoes by pulse to pulse with (20) for different slow time.
- 9) Repeat 4)–8) to generate the bistatic SAR echo data of the undulating terrain.

At last, considering that time domain BP imaging algorithm [54], [55], [56], [57] has no restrictions of geometry configuration for bistatic SAR, it is used to process the simulated raw data to validate the effectiveness of the proposed framework.

#### V. SIMULATED AND MEASURED DATA EXPERIMENTS

In order to verify the effectiveness of the bistatic SAR raw data simulation framework proposed in this article, different numerical simulated and measured data experiments are carried out in this section.

##### A. Simulated Circular Mound Undulating Terrain Experiment

The circular mound undulating terrain is a relatively common and ideal terrain, so the simulation experiments can illustrate the effectiveness of the proposed framework. Fig. 7 shows the simulated rolling mound terrain, the height of the top of the

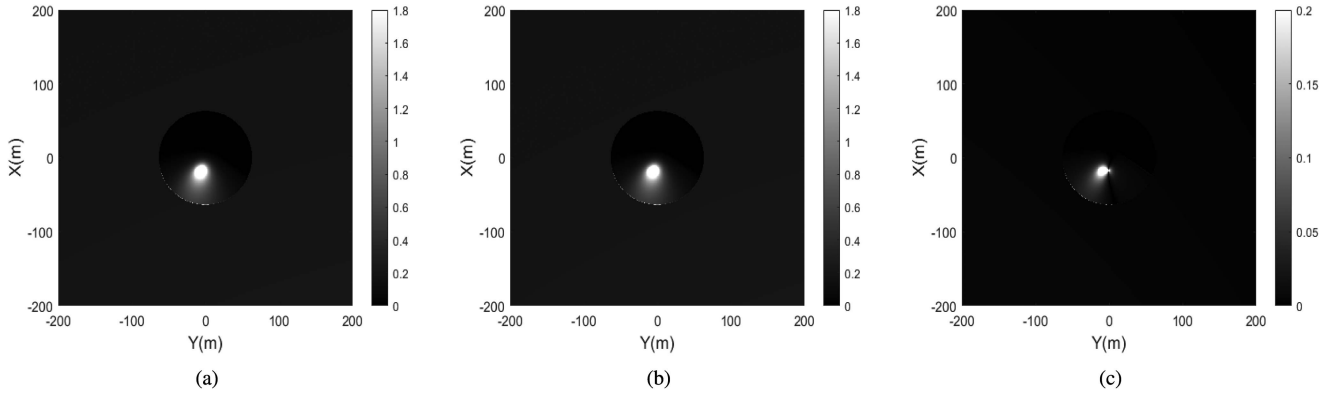


Fig. 8. Scattering coefficients at different slow times. (a)  $t = 2.67$  s. (b)  $t = 3.33$  s. (c) Difference between (a) and (b).

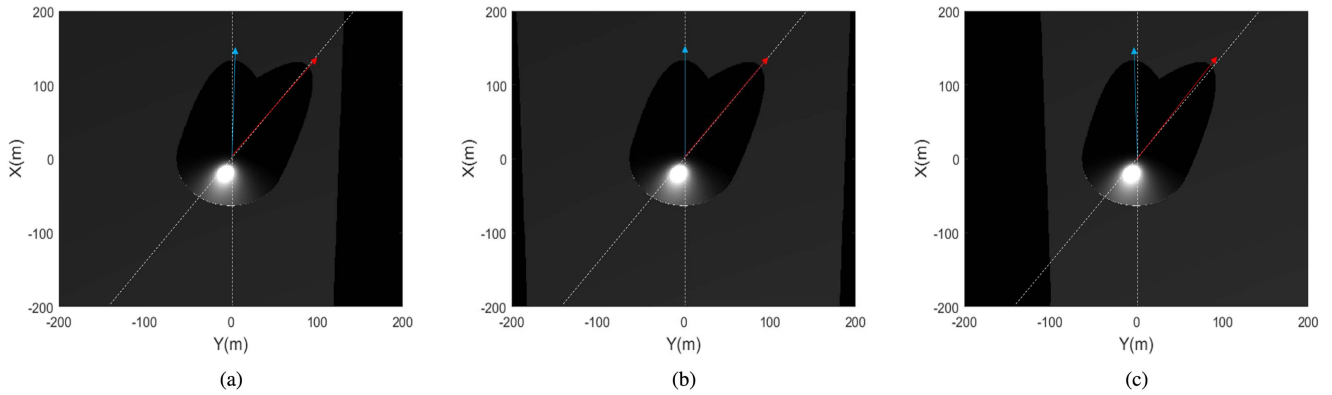


Fig. 9. Shadow variations at different slow times. (a)  $t = 2.99$  s. (b)  $t = 3.41$  s. (c)  $t = 3.97$  s.

TABLE II  
SIMULATION PARAMETERS

Carrier Frequency	10GHz
Polarization mode	HH
Location of transmitter at aperture center	(-6,-4,6)km
Velocity of transmitter	(0,150,0)m/s
Location of receiver at aperture center	(-3,0,3)km
Velocity of receiver	(0,150,0)m/s

mound is 120 m, the size of the entire scene area is  $400 \times 400$  m, and the size of facet is  $0.5 \times 0.5$  m. The transmitter and receiver fly in parallel at the same speed, with the transmitter in squint-looking mode and the receiver in side-looking mode, and partial parameters for scattering coefficient computation are listed in Table II.

Fig. 8 depicts the results of the scene scattering coefficients calculated at different slow times and the difference between them. It can be seen that the scattering coefficients of the scene are changing as the aircraft moves, which is in line with the practical feature that the scattering coefficients of the targets are different in different directions. Fig. 9 shows the judgment results of the shadows at different azimuth times. Since the

shadow judgment method takes into account the influence of beam width, the SAR beam irradiation range is a limited area, and the area outside the beam can be directly regarded as a shadow area. In addition, the red arrow in Fig. 9 indicates the direction of transmitter shadow and the blue arrow indicates the direction of receiver shadow, and two white dashed lines are auxiliary reference lines to better observe the changes in shadow direction of transmitter and receiver at different azimuth times. Besides, due to the large azimuth angle difference between the transmitter and receiver to the center of the scene, an obvious double-shadow phenomenon can be seen in Fig. 9.

According to the analysis in Section III, the double shadow is closely related to the size of the azimuth and elevation angles, but mainly depends on the size of the azimuth angle difference. For example, when the azimuth angle of the transmitting and receiving stations is the same, double shadows will never appear. Generally, the greater the difference in azimuth angle, the wider the separation of shadows between the transmitting and receiving stations, and the more likely there is a double shadow phenomenon, hence, the simulation results with different azimuth differences are illustrated in Fig. 10. It should be noted that the result does not include the procedure of coherent superposition of echoes from different facets, hence speckle phenomenon cannot be observed here. As shown in Fig. 10(a), when the azimuth angle difference is 0, one of the shadows



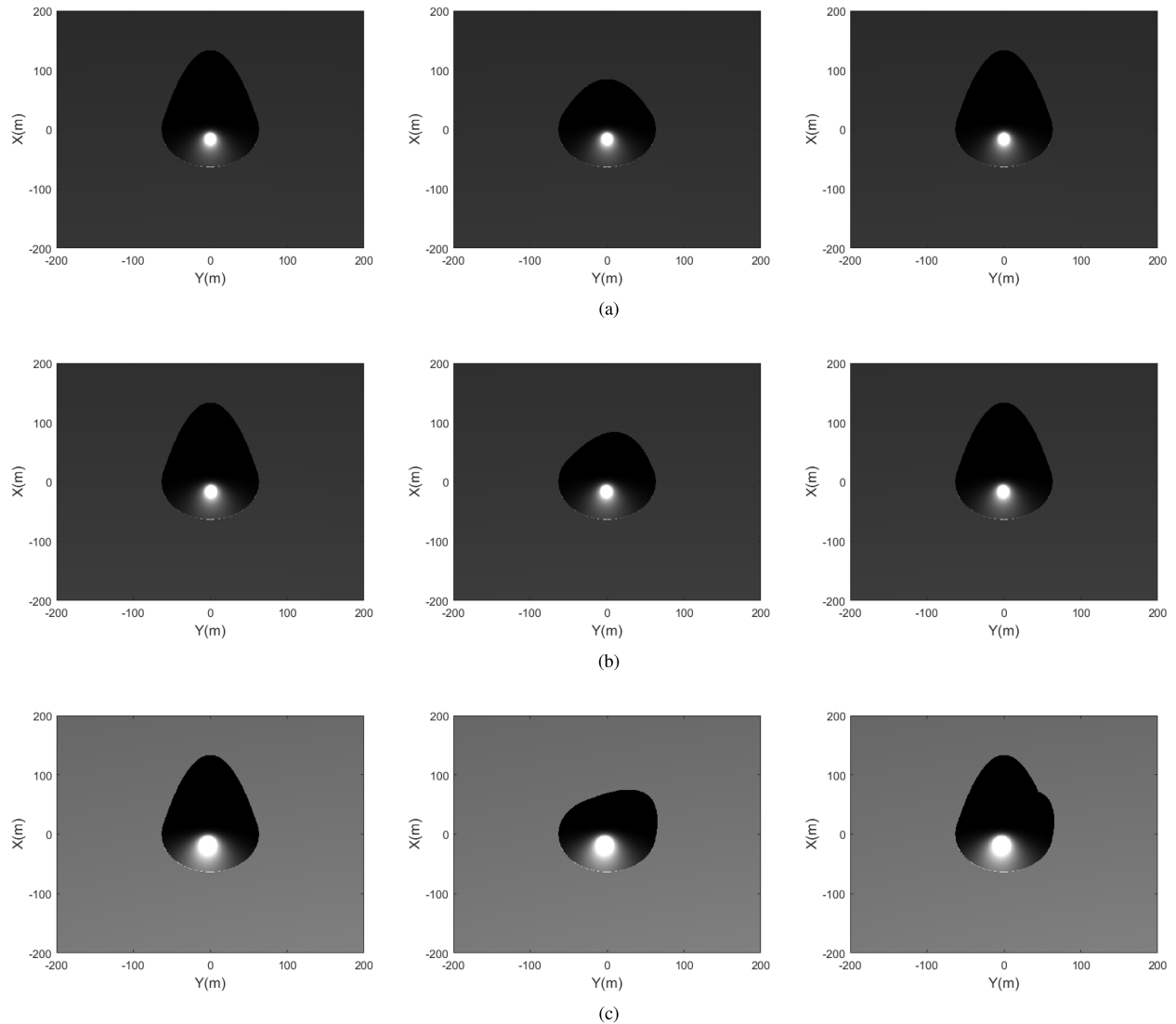


Fig. 10. Shadow simulation results under different conditions. (a)  $\Delta\beta = 0^\circ$ ,  $\Delta\gamma = 15^\circ$ . (b)  $\Delta\beta = 10^\circ$ ,  $\Delta\gamma = 15^\circ$ . (c)  $\Delta\beta = 35^\circ$ ,  $\Delta\gamma = 15^\circ$ . (From left to right) Subimages in every row correspond to the shadow of transmitting station, shadow of receiving station, final shadow results, respectively.

is completely covered by the other due to the same direction of the two shadows, and only one shadow is presented. From Fig. 10(b), it can be found that as the azimuth angles of the transmitting and receiving stations change, the direction of the shadow also changes. However, due to the small shadowing range of the receiving station, it is completely covered by the shadowing area of the transmitting station, and thus, the final result is also presented as a single shadow. When the azimuth angle difference is larger, as shown in Fig. 10(c), the transmitting station shadow cannot completely cover the receiving station shadow, and a clear double-shadow phenomenon appears at this time. In general, the simulation results shown above are consistent with the theoretical analysis, which indicates the effectiveness of the proposed simulation framework.

### B. DEM Experiment

In order to verify the effectiveness of the proposed framework, raw data simulation is performed using provided digital

elevation data, where the size of facet is  $1 \times 1$  m, the scene size is  $1200 \times 600$  m, and the scene elevation information is shown in Fig. 11.

The red arrow and black arrow in the figure are the trajectory of transmitter and receiver, respectively. The SAR configuration is bistatic forward-looking, where the transmitter irradiates the scene with squint-looking, and the receiver with forward-looking, and system simulation parameters are shown in Table III.

According to the proposed simulation framework, the scattering coefficient of the scene is calculated at each azimuth moment, and the 2-D echo data are obtained after traversing all azimuth moments. Then, the BP algorithm is used for imaging the generated echo data to verify effectiveness of the proposed simulated framework and the results are shown in Fig. 12, where Fig. 12(a) shows the simulated bistatic SAR raw data of the scene, and Fig. 12(b) shows the imaging results of the simulated raw data. It can be seen that the result can reflect the scattering characteristics of the undulating terrain, and the

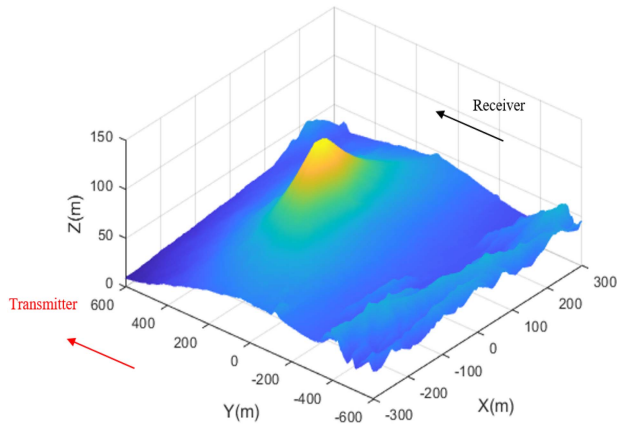


Fig. 11. Digital elevation map of undulating terrain.

TABLE III  
SIMULATION PARAMETERS

Carrier frequency	10 GHz	
Polarization mode	HH	
Pulse duration	5 $\mu$ s	
Bandwidth	150 MHz	
Range sampling frequency	180 MHz	
Pulse repetition frequency	500 Hz	
Synthetic aperture time	1 s	
Configuration parameters	Translational invariant Mode	Translational invariant Mode
Location of transmitter at aperture center	(-6,-4,1.5) km	(4,-6,1.5) km
Velocity of transmitter	(0,150,0) m/s	(-150,0,0) m/s
Location of receiver at aperture center	(0,-3,1) km	(0,-3,1) km
Velocity of receiver	(0,150,0) m/s	(0,150,0) m/s

double shadow phenomenon appears in the red rectangle domain of Fig. 12(b). Besides, there are also obvious foreshortening and layover phenomena, for example, the position of mountain peak in the imaging result has shifted and is no longer located at the horizontal center of the image due to the conversion between slant-distance and ground distance, which indicates that the results can effectively simulate the real echo acquisition process.

To further verify the effectiveness of the proposed framework, we added some strong scattering targets to the scene and let the transmitter fly along different trajectories shown in Fig. 13 to observe the imaging results. Fig. 14(a) shows the result that the transmitter flies along the trajectory 1, and Fig. 14(b) presents the result that the transmitter flies along the trajectory 2. As can be seen from the imaging results, the resolution is different, and the shadow occlusion phenomenon changes due to the different bistatic configuration, and most of the strong scattering targets cannot be observed due to the shadow of the mountain in the result that the transmitter flies along trajectory 2. The imaging results of different bistatic SAR configurations indicate that raw data simulation framework is effective and it can help to verify the effectiveness of different configuration designs, which is also an important research topic in bistatic SAR [58].

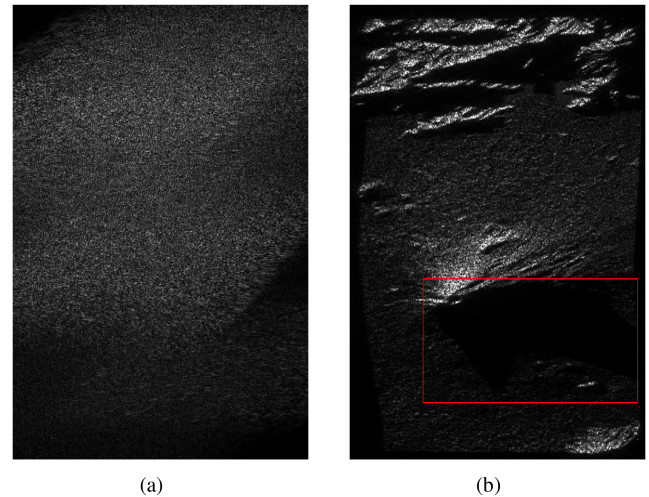


Fig. 12. Simulated bistatic SAR echo and corresponding imaging result. (a) Amplitude information of echo data. (b) Imaging result.

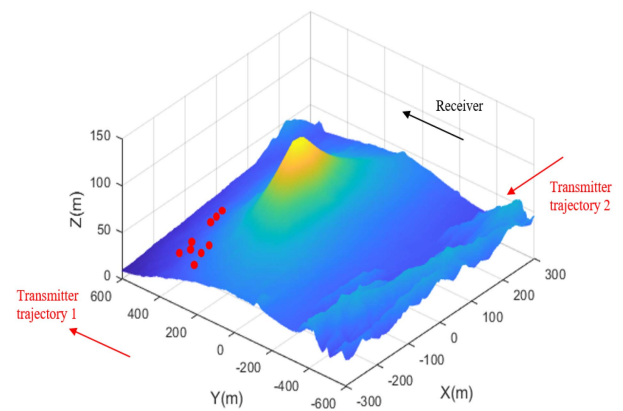


Fig. 13. Digital elevation map with strong scattering targets.

Besides, in order to illustrate the difference between monostatic SAR and bistatic SAR, the imaging result of monostatic SAR that flies along the trajectory 1 is shown in Fig. 15. Comparing the results in Figs. 14 and 15, it can be found that due to the difference of geometric configuration, the scattering characteristics and imaging resolution of the scene under the bistatic SAR configuration are quite different with that of monostatic SAR. Especially, the shadow phenomenon has undergone significant changes, where only one shadow appears in the rectangular box. All the above findings are consistent with theoretical understanding, which further demonstrates the effectiveness of the proposed simulation framework.

### C. Comparisons

In order to further illustrate the effectiveness of the proposed scheme, the comparisons are made in this part. Considering that the shadow judgment with ray tracing [41] and the simulation algorithm with time-domain pulse by pulse calculation [7] own

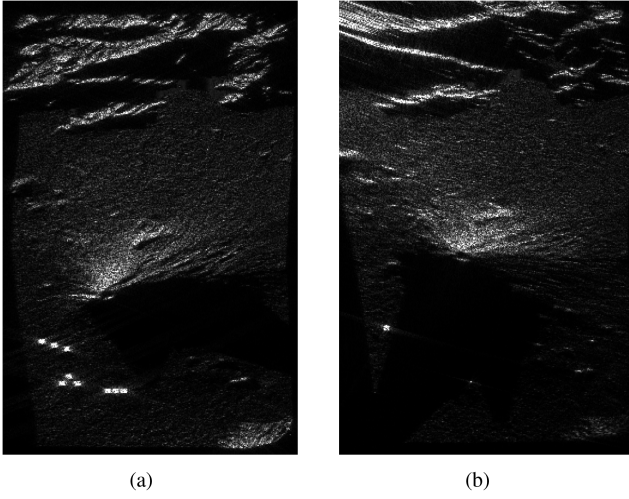


Fig. 14. Imaging results of simulated bistatic SAR raw data. (a) Transmitter is trajectory 1. (b) Transmitter is trajectory 2.

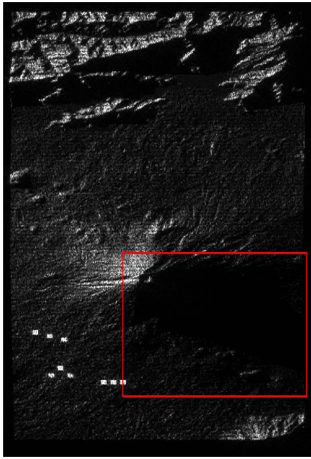


Fig. 15. Imaging result of simulated monostatic SAR raw data with trajectory 1.

the highest accuracy, they are used to simulate the raw data first, and BP imaging is conducted on the raw data to get the benchmark for comparisons, just as shown in Fig. 16.

Comparing Fig. 16 with Figs. 12(b) and 14(b), respectively, it can be seen that the imaging results of the simulated raw data with different schemes are basically consistent. Besides, the structure similarity index measure (SSIM) [59] is used to quantitatively evaluate the similarity of the two sets of images, which can be calculated as follows:

$$\text{SSIM}(x, y) = [l(x, y)]^\alpha [c(x, y)]^\beta [s(x, y)]^\gamma \quad (23)$$

where  $x$  and  $y$  are the two images.  $\alpha$ ,  $\beta$ , and  $\gamma$  are constants and are usually set to 1 in real engineering.  $l(x, y)$ ,  $c(x, y)$ , and  $s(x, y)$  are functions of brightness, contrast, and structure, respectively, and the corresponding calculation formulas are as

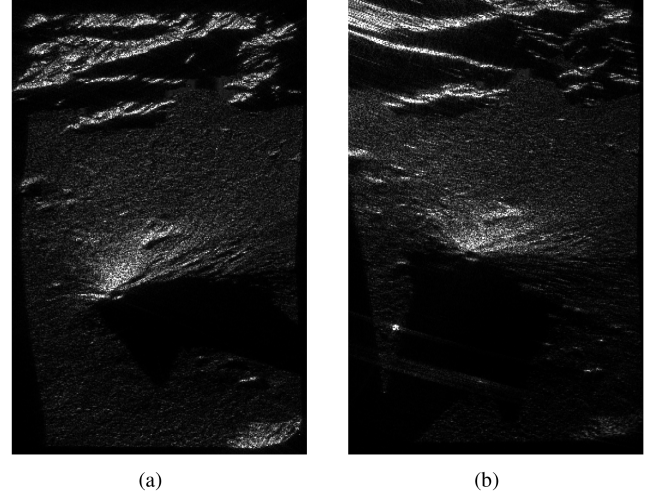


Fig. 16. Benchmark for the comparisons. (a) Transmitter is trajectory 1. (b) Transmitter is trajectory 2.

follows:

$$\begin{cases} l(x, y) = (2\mu_x\mu_y + c_1)/(\mu_x^2 + \mu_y^2 + c_1) \\ c(x, y) = (2\sigma_{xy} + c_2)/(\sigma_x^2 + \sigma_y^2 + c_2) \\ s(x, y) = (\sigma_{xy} + c_3)/(\sigma_x\sigma_y + c_3). \end{cases} \quad (24)$$

Among them,  $\mu_x$  and  $\mu_y$  represent the average, and  $\sigma_x$  and  $\sigma_y$  are variance of  $x$  and  $y$ , respectively, and  $\sigma_{xy}$  is the covariance of  $x$  and  $y$ .  $c_1$ ,  $c_2$ , and  $c_3$  are constants to avoid system errors caused by a denominator of 0, and corresponding calculation formulas are as follows:

$$\begin{cases} c_1 = (k_1L)^2 \\ c_2 = (k_2L)^2 \\ c_3 = c_2/2 \end{cases} \quad (25)$$

where  $k_1$  and  $k_2$  are constants and are usually set to 0.01 and 0.03 in real engineering,  $L$  represents the maximum grayscale of the image. The value range is  $\text{SSIM} \in [0, 1]$ , and the larger the value, the higher similarity between two images. After calculation, the SSIM value of the Figs. 16(a) and 12(b) and the SSIM value of Figs. 16(b) and 14(b) are both greater than 0.97, which means that the structure of the two sets of images are highly similar. As for the degree of efficiency improvement, it depends on how many facets are on the same or approximately the same ground projection line. Generally, the more approximations there are, the higher the efficiency improvement. Of course, there may also be a certain loss in the accuracy of shadow judgment. Under the conditions of DEM and simulation parameters used in the article, and based on the shadow judgment time spent at each azimuth moment, the efficiency of the proposed scheme is better than that of the ray tracing scheme by approximately ten times.

#### D. Discussions About Speckle Noise

Speckle noise is an important phenomenon in SAR image. In principle, speckle noise is formed by the coherent superposition of scattered echoes from different small facets within the same resolution cell. Hence, as long as the size of the facet is smaller

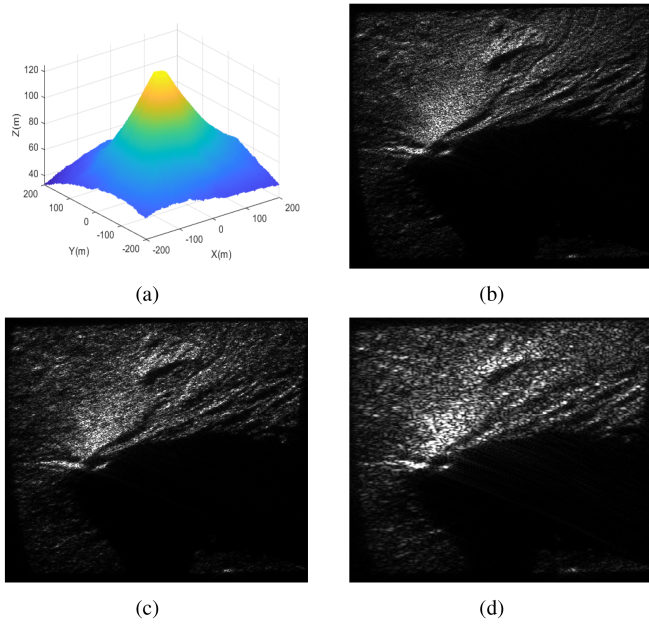


Fig. 17. DEM and imaging results of corresponding simulated raw data with different facets and resolution cells. (a) DEM of undulating terrain. (b) Facet size:  $1 \times 1$  m; Resolution cell:  $1.25 \times 1$  m. (c) Facet size:  $0.25 \times 0.25$  m; Resolution cell:  $1.25 \times 1$  m. (d) Facet size:  $1 \times 1$  m; Resolution cell:  $3 \times 3$  m.

than the resolution cell determined by SAR system parameters, speckle noise will form, and its difference mainly depends on the size of the facet relative to the resolution cell. Generally speaking, the smaller the facet relative to the resolution cell, the more obvious the speckle noise, and vice versa. Of course, the smaller the facets, the greater the computational complexity it brings. In practice, the choice of facet number is usually a compromise between simulation accuracy and computational efficiency. To illustrate the influence of the relative relationship between the facet size and the resolution cell on speckle, partial area in Fig. 11 are chosen for simulation, as shown in Fig. 17(a), and the simulation parameters are the same as Table III. Then, with different facet sizes and resolution cells, the raw data are simulated and the corresponding imaging results are shown in Fig. 17(b)–(d), where Fig. 17(b) is the case with facet size:  $1 \times 1$  m and resolution cell:  $1.25 \times 1$  m, Fig. 17(c) is the case with facet size:  $0.25 \times 0.25$  m and resolution cell:  $1.25 \times 1$  m, Fig. 17(d) is the case with facet size:  $1 \times 1$  m and resolution cell:  $3 \times 3$  m. It can be seen that the larger the resolution cell relative to the facet size, the more obvious the speckle phenomenon, which is consistent with theoretical analysis.

### E. Simulation Results Including Platform Error

According to the simulation process above, most operations are completed in the time domain, it can effectively embed the errors of platform. To illustrate this point, we have added a set of simulation results for embedding motion errors, and provided imaging results using ideal trajectories and actual trajectories, respectively, to demonstrate the effectiveness of simulated raw data with errors. Just as shown in Figs. 18–20, which are the used DEM, the actual trajectories of transmitting and receiving

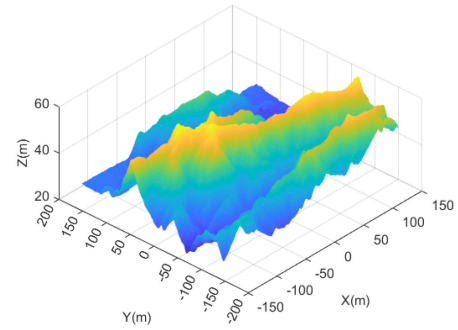


Fig. 18. Digital elevation map of actual terrain.

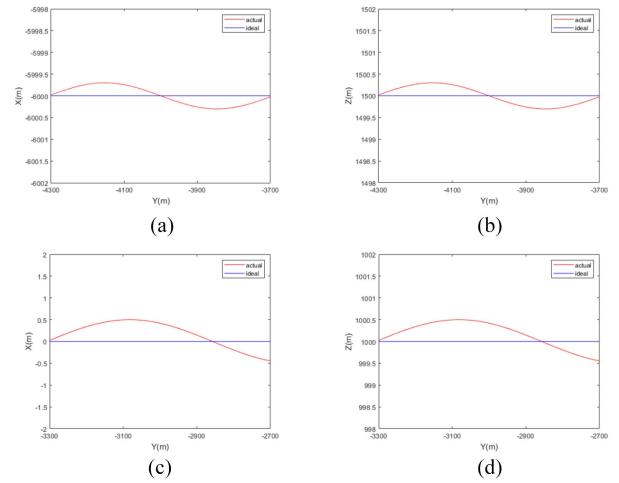


Fig. 19. Actual and ideal trajectories of transmitting and receiving platform. (a) XOY plane of transmitting platform. (b) YOZ plane of transmitting platform. (c) XOY plane of receiving platform. (d) YOZ plane of receiving platform.

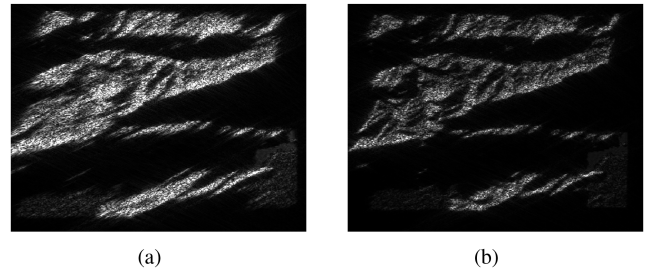


Fig. 20. Imaging results of simulated data. (a) With ideal trajectory. (b) With actual trajectory.

platforms, and the imaging results with ideal trajectory and actual trajectory, respectively. It should be pointed out that this manuscript does not involve specific motion compensation methods. In principle, when the actual trajectories are used for imaging, it actually implicitly compensates for the nonideal motion of the platform, while imaging with ideal trajectories is equivalent to not compensating for the influence of platform errors.

It can be seen that when the ideal trajectory is used for imaging, defocusing problems will occur due to the mismatch

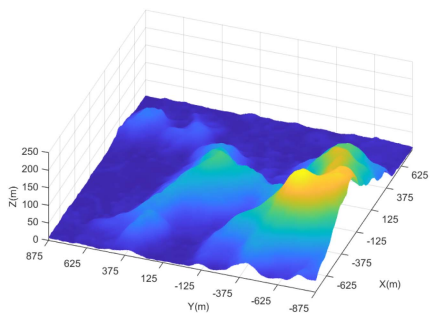


Fig. 21. Digital elevation map of actual terrain.

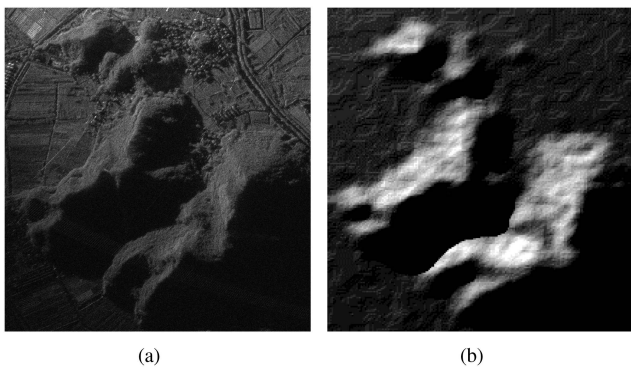


Fig. 22. Bistatic SAR image. (a) Measured SAR image. (b) Imaging result of simulated bistatic SAR raw data.

between the actual trajectory and ideal trajectory, while good focus can be achieved if the actual trajectory is used, which indicates that the simulated raw data effectively embeds the influence of motion errors.

#### F. Measured Data Experiment

Measured data results are given in this part to further illustrate the effectiveness of the proposed framework. In December 2020, with the GF-3 satellite as the transmitting platform, the Cessna aircraft as a receiving platform, the satellite/aircraft bistatic SAR experiment at C band is conducted in Zhoushan, Zhejiang, and the DEM of the measured scene is shown in Fig. 21.

During the experiment, the transmitting antenna is almost side-looking, and the receiving antenna is squint-looking. More specific information about this experiment and bistatic SAR system can be obtained in [60]. The imaging result with BP algorithm is shown in Fig. 22, where Fig. 22(a) is the measured bistatic SAR image of the scene, Fig. 22(b) presents the BP imaging result of the simulated bistatic SAR raw data with the proposed framework. It can be seen that although the imaging result of simulated bistatic SAR raw data cannot fully represent the actual distribution of ground objects due to the accuracy limitations of DEM and geometric distortion phenomenon, it can reflect the contours of the terrain, which is basically consistent with the measured bistatic SAR image, which further illustrates the effectiveness of the proposed framework. Besides, the simulated results can assist in SAR image registration, geometric correction, etc. [61].

## VI. CONCLUSION

With time-varying scattering coefficient acquisition based on the scattering model of bistatic radar and the prior information of DEM data, the shadow judgement based on facet cell fitting and elevation angle comparison, and the echo simulation based on pulse by pulse in time domain, a framework of bistatic SAR raw data simulation under undulating terrain is proposed in this article, and it is verified through simulation and measured data experiments. Because of the consideration of the impact of terrain fluctuations, the simulation results of the proposed framework are closer to the actual situation, especially in simulating the shadow occlusion and possible double shadow phenomena of bistatic SAR, which will provide a good foundation for bistatic SAR task design, trajectory planning, algorithm validation, etc. Besides, since the whole simulation process is conducted in time domain, the framework has no limitations on the geometry configurations of bistatic SAR.

## REFERENCES

- [1] G. Franceschetti, M. Migliaccio, D. Riccio, and G. Schirinzi, "SARAS: A synthetic aperture radar (SAR) raw signal simulator," *IEEE Trans. Geosci. Remote Sens.*, vol. 30, no. 1, pp. 110–123, Jan. 1992.
- [2] O. Dogan and M. Kartal, "Efficient strip-mode SAR raw-data simulation of fixed and moving targets," *IEEE Geosci. Remote Sens. Lett.*, vol. 8, no. 5, pp. 884–888, Sep. 2011.
- [3] R. Scheiber, M. Pinheiro, M. Rodriguez-Cassola, and P. Prats, "Spaceborne bistatic SAR scene simulation," in *Proc. IEEE Int. Geosci. Remote Sens. Symp.*, 2018, pp. 4459–4462.
- [4] Y. Li, W. Li, Z. Sun, J. Wu, Z. Li, and J. Yang, "An autofocus scheme of bistatic SAR considering cross-cell residual range migration," *IEEE Geosci. Remote Sens. Lett.*, vol. 19, 2022, Art. no. 4507905.
- [5] W. Pu et al., "Motion errors and compensation for bistatic forward-looking SAR with cubic-order processing," *IEEE Trans. Geosci. Remote Sens.*, vol. 54, no. 12, pp. 6940–6957, Dec. 2016.
- [6] W. Li, J. Yang, Y. Huang, and J. Wu, "A geometry-based Doppler centroid estimator for bistatic forward-looking SAR," *IEEE Geosci. Remote Sens. Lett.*, vol. 9, no. 3, pp. 388–392, May 2012.
- [7] A. Mori and F. De Vita, "A time-domain raw signal simulator for interferometric SAR," *IEEE Trans. Geosci. Remote Sens.*, vol. 42, no. 9, pp. 1811–1817, Sep. 2004.
- [8] O. Dogan and M. Kartal, "Time domain SAR raw data simulation of distributed targets," *EURASIP J. Adv. Signal Process.*, vol. 2010, 2010, Art. no. 784815.
- [9] D. Li, M. Rodriguez-Cassola, P. Prats-Iraola, M. Wu, and A. Moreira, "Reverse backprojection algorithm for the accurate generation of SAR raw data of natural scenes," *IEEE Geosci. Remote Sens. Lett.*, vol. 14, no. 11, pp. 2072–2076, Nov. 2017.
- [10] F. Zhang, X. Yao, H. Tang, Q. Yin, Y. Hu, and B. Lei, "Multiple mode SAR raw data simulation and parallel acceleration for Gaofen-3 mission," *IEEE J. Sel. Topics Appl. Earth Observ. Remote Sens.*, vol. 11, no. 6, pp. 2115–2126, Jun. 2018.
- [11] G. D. Martino, A. Iodice, A. Natale, and D. Riccio, "Time-domain and monostatic-like frequency-domain methods for bistatic SAR simulation," *Sensors*, vol. 21, 2021, Art. no. 5012.
- [12] A. S. Khwaja, L. Ferro-Famil, and E. Pottier, "Efficient SAR raw data generation for anisotropic urban scenes based on inverse processing," *IEEE Geosci. Remote Sens. Lett.*, vol. 6, no. 4, pp. 757–761, Oct. 2009.
- [13] L. Yang, W. Yu, S. Zheng, and L. Zhang, "Efficient bistatic SAR raw signal simulator of extended scenes," *Int. J. Antennas Propag.*, vol. 2014, 2014, Art. no. 130784.
- [14] Z. Meng, Y. Li, C. Li, M. dao Xing, and Z. Bao, "A raw data simulator for bistatic forward-looking high-speed maneuvering-platform SAR," *Signal Process.*, vol. 117, pp. 151–164, 2015.
- [15] Z. Guo, Z. Fu, J. Chang, L. Wu, and N. Li, "A novel high-squint spotlight SAR raw data simulation scheme in 2-D frequency domain," *Remote Sens.*, vol. 14, no. 3, 2022, Art. no. 651.

- [16] X. Qiu, D. Hu, L. Zhou, and C. Ding, "A bistatic SAR raw data simulator based on inverse  $\omega-k$  algorithm," *IEEE Trans. Geosci. Remote Sens.*, vol. 48, no. 3, pp. 1540–1547, Mar. 2010.
- [17] A. S. Khwaja, L. Ferro-Famil, and E. Pottier, "Efficient stripmap SAR raw data generation taking into account sensor trajectory deviations," *IEEE Geosci. Remote Sens. Lett.*, vol. 8, no. 4, pp. 794–798, Jul. 2011.
- [18] M. Vandewal, R. Speck, and H. Suss, "Efficient SAR raw data generation including low squint angles and platform instabilities," *IEEE Geosci. Remote Sens. Lett.*, vol. 5, no. 1, pp. 26–30, Jan. 2008.
- [19] G. Fornaro, E. Sansosti, R. Lanari, and M. Tesauro, "Role of processing geometry in SAR raw data focusing," *IEEE Trans. Aerosp. Electron. Syst.*, vol. 38, no. 2, pp. 441–454, Apr. 2002.
- [20] H. Xu, Z. Yang, G. Chen, G. Liao, and M. Tian, "A ground moving target detection approach based on shadow feature with multichannel high-resolution synthetic aperture radar," *IEEE Geosci. Remote Sens. Lett.*, vol. 13, no. 10, pp. 1572–1576, Oct. 2016.
- [21] D. Brunner, G. Lemoine, L. Bruzzone, and H. Greidanus, "Building height retrieval from VHR SAR imagery based on an iterative simulation and matching technique," *IEEE Trans. Geosci. Remote Sens.*, vol. 48, no. 3, pp. 1487–1504, Mar. 2010.
- [22] W. Li et al., "An improved iterative simulation and matching scheme for building height retrieval from SAR image," *IEEE Geosci. Remote Sens. Lett.*, vol. 20, 2023, Art. no. 4007905.
- [23] W. Li, Z. Wang, R. Chen, Z. Li, J. Wu, and J. Yang, "Traditional synthetic aperture processing assisted GAN-like network for multichannel radar forward-looking superresolution imaging," *IEEE Trans. Geosci. Remote Sens.*, vol. 62, 2024, Art. no. 5201813.
- [24] W. Li et al., "LRSD-ADMM-Net: Simultaneous super-resolution imaging and target detection for forward-looking scanning radar," *IEEE J. Sel. Topics Appl. Earth Observ. Remote Sens.*, vol. 17, pp. 4052–4061, 2024.
- [25] X. Pan, L. Kang, B. Zou, Y. Zhang, and L. Zhang, "High-resolution SAR signal simulation using parallel FDTD method," in *Proc. IEEE Geosci. Remote Sens. Symp.*, 2014, pp. 490–493.
- [26] P. Peng, L. X. Guo, and C. Tong, "An em model for radar multipath simulation and HRRP analysis of low altitude target above electrically large composite scale rough surface," *Electromagnetics*, vol. 38, pp. 177–188, 2018.
- [27] J. C. Landy, M. Tsamados, and R. K. Scharien, "A facet-based numerical model for simulating SAR altimeter echoes from heterogeneous sea ice surfaces," *IEEE Trans. Geosci. Remote Sens.*, vol. 57, no. 7, pp. 4164–4180, Jul. 2019.
- [28] W. Xia and J. Zhou, "Typical terrain SAR echo simulation and SAR image simulation," *J. Remote Sens.*, vol. 13, no. 3, pp. 404–410, 2009, doi: 10.11834/jrs.20090305.
- [29] G. Jing, Y. Zhang, S. Guang-Cai, and Z. Bao, "Fast method for SAR echo simulation of a three-dimensional ground scene," *Xi'an Dianzi Keji Daxue Xuebao/J. Xidian Univ.*, vol. 44, no. 33, pp. 1–7, 2017.
- [30] Y. Shen, X. Wang, H. Chen, and X. Hao, "SAR raw echo simulation of ground scene," in *Proc. 3rd Int. Congr. Image Signal Process.*, 2010, vol. 5, pp. 2251–2254.
- [31] G. Franceschetti, M. Migliaccio, and D. Riccio, "On ocean SAR raw signal simulation," *IEEE Trans. Geosci. Remote Sens.*, vol. 36, no. 1, pp. 84–100, Jan. 1998.
- [32] B. Liu and Y. He, "SAR raw data simulation for ocean scenes using inverse Omega-K algorithm," *IEEE Trans. Geosci. Remote Sens.*, vol. 54, no. 10, pp. 6151–6169, Oct. 2016.
- [33] T. Zeng, C. Hu, H. Sun, and E. Chen, "A novel rapid SAR simulator based on equivalent scatterers for three-dimensional forest canopies," *IEEE Trans. Geosci. Remote Sens.*, vol. 52, no. 9, pp. 5243–5255, Sep. 2014.
- [34] G. Franceschetti and D. Riccio, *Scattering, Natural Surfaces, and Fractals*. London, U.K.: Academic Press, 2007, pp. 13–15.
- [35] A. Di Simone et al., "Analytical models for the electromagnetic scattering from isolated targets in bistatic configuration: Geometrical optics solution," *IEEE Trans. Geosci. Remote Sens.*, vol. 58, no. 2, pp. 861–880, Feb. 2020.
- [36] F. T. Ulaby, R. K. Moore, and A. K. Fung, *Microwave Remote Sensing: Active and Passive (Microwave Remote Sensing Fundamentals and Radiometry)*, vol. 1. Norwood, MA, USA: Artech House Publishers, 1981.
- [37] K. Chen, T.-D. Wu, L. Tsang, Q. Li, J. Shi, and A. Fung, "Emission of rough surfaces calculated by the integral equation method with comparison to three-dimensional moment method simulations," *IEEE Trans. Geosci. Remote Sens.*, vol. 41, no. 1, pp. 90–101, Jan. 2003.
- [38] A. G. Voronovich and V. U. Zavorotny, "Full-polarization modeling of monostatic and bistatic radar scattering from a rough sea surface," *IEEE Trans. Antennas Propag.*, vol. 62, no. 3, pp. 1362–1371, Mar. 2014.
- [39] G. Di Martino, A. Di Simone, A. Iodice, and D. Riccio, "Bistatic scattering from anisotropic rough surfaces via a closed-form two-scale model," *IEEE Trans. Geosci. Remote Sens.*, vol. 59, no. 5, pp. 3656–3671, May 2021.
- [40] Y. Zhang, "Study on the electromagnetic scattering characteristics and engineering statistical model of typical land surface," Ph.D. dissertation, Dept. Radio Phys., Xidian Univ., Xian, China, 2017, pp. 104–109.
- [41] S. Auer, S. Hinz, and R. Bamler, "Ray-tracing simulation techniques for understanding high-resolution SAR images," *IEEE Trans. Geosci. Remote Sens.*, vol. 48, no. 3, pp. 1445–1456, Mar. 2010.
- [42] Z. Chen, Z. Zeng, Y. Huang, J. Wan, and X. Tan, "SAR raw data simulation for fluctuant terrain: A new shadow judgment method and simulation result evaluation framework," *IEEE Trans. Geosci. Remote Sens.*, vol. 60, 2022, Art. no. 5215018.
- [43] V. B. S. Prasath and O. Haddad, "Radar shadow detection in synthetic aperture radar images using digital elevation model and projections," *J. Appl. Remote Sens.*, vol. 8, no. 01, 2014, Art. no. 1.
- [44] A. F. Habib, E. M. Kim, and C. Kim, "New methodologies for true orthophoto generation," *Photogrammetric Eng. Remote Sens.*, vol. 73, pp. 25–36, 2007.
- [45] Z. Li, J. Wu, Q. Yi, Y. Huang, and J. Yang, "An Omega- $k$  imaging algorithm for translational variant bistatic SAR based on linearization theory," *IEEE Geosci. Remote Sens. Lett.*, vol. 11, no. 3, pp. 627–631, Mar. 2014.
- [46] Y. Li, T. Zhang, H. Mei, Y. Quan, and M. Xing, "Focusing translational-variant bistatic forward-looking SAR data using the modified Omega-K algorithm," *IEEE Trans. Geosci. Remote Sens.*, vol. 60, 2022, Art. no. 5203916.
- [47] Y. L. Neo, F. H. Wong, and I. G. Cumming, "Processing of azimuth-invariant bistatic SAR data using the range Doppler algorithm," *IEEE Trans. Geosci. Remote Sens.*, vol. 46, no. 1, pp. 14–21, Jan. 2008.
- [48] R. Wang, O. Loffeld, H. Nies, S. Knedlik, and J. H. G. Ender, "Chirp-scaling algorithm for bistatic SAR data in the constant-offset configuration," *IEEE Trans. Geosci. Remote Sens.*, vol. 47, no. 3, pp. 952–964, Mar. 2009.
- [49] T. Zhang, Y. Li, J. Wang, M. Xing, L. Guo, and P. Zhang, "A modified range model and extended Omega-K algorithm for high-speed-high-squint SAR with curved trajectory," *IEEE Trans. Geosci. Remote Sens.*, vol. 61, 2023, Art. no. 5204515.
- [50] Y. Li, G. Xu, S. Zhou, M. Xing, and X. Song, "A novel CFFBP algorithm with noninterpolation image merging for bistatic forward-looking SAR focusing," *IEEE Trans. Geosci. Remote Sens.*, vol. 60, 2022, Art. no. 5225916.
- [51] G. Franceschetti, A. Iodice, D. Riccio, and G. Ruello, "SAR raw signal simulation for urban structures," *IEEE Trans. Geosci. Remote Sens.*, vol. 41, no. 9, pp. 1986–1995, Sep. 2003.
- [52] W. Li et al., "A shadow simulation scheme for SAR images of undulating terrain based on facet cell fitting and elevation angle comparison," *IEEE Geosci. Remote Sens. Lett.*, vol. 20, 2023, Art. no. 4003505.
- [53] H. C. de Oliveira, A. P. D. Poz, M. Galo, and A. F. Habib, "Surface gradient approach for occlusion detection based on triangulated irregular network for true orthophoto generation," *IEEE J. Sel. Topics Appl. Earth Observ. Remote Sens.*, vol. 11, no. 2, pp. 443–457, Feb. 2018.
- [54] A. Focsa, A. Anghel, and M. Datcu, "Accelerated back-projection SAR processor on arbitrary elliptical imaging grid with azimuth spectrum unfolding," *IEEE Geosci. Remote Sens. Lett.*, vol. 20, 2023, Art. no. 4008005.
- [55] G. Qian, Y. Wang, B. Zhang, and M. Liu, "Bistatic forward-looking SAR imaging of uniformly moving target based on improved bp algorithm," *IEEE Trans. Comput. Imag.*, vol. 9, pp. 1006–1017, 2023.
- [56] W. Li, R. Chen, J. Yang, J. Wu, Y. Zhang, and Y. Huang, "A hybrid real/synthetic aperture scheme for multichannel radar forward-looking superresolution imaging," *IEEE Geosci. Remote Sens. Lett.*, vol. 20, 2023, Art. no. 3507505.
- [57] D. Feng, D. An, and X. Huang, "An extended fast factorized back projection algorithm for missile-borne bistatic forward-looking SAR imaging," *IEEE Trans. Aerosp. Electron. Syst.*, vol. 54, no. 6, pp. 2724–2734, Dec. 2018.
- [58] Z. Sun, J. Wu, J. Yang, Y. Huang, C. Li, and D. Li, "Path planning for GEO-UAV bistatic SAR using constrained adaptive multiobjective differential evolution," *IEEE Trans. Geosci. Remote Sens.*, vol. 54, no. 11, pp. 6444–6457, Nov. 2016.
- [59] L. Fei, L. Yan, C. Chen, Z. Ye, and J. Zhou, "OSSIM: An object-based multiview stereo algorithm using SSIM index matching cost," *IEEE Trans. Geosci. Remote Sens.*, vol. 55, no. 12, pp. 6937–6949, Dec. 2017.

- [60] Z. Sun et al., "Spaceborne-airborne bistatic SAR experiment using GF-3 illuminator: Description, processing and results," in *Proc. IEEE Int. Geosci. Remote Sens. Symp.*, 2021, pp. 2699–2702.
- [61] M. Shimada, "Ortho-rectification and slope correction of SAR data using DEM and its accuracy evaluation," *IEEE J. Sel. Topics Appl. Earth Observ. Remote Sens.*, vol. 3, no. 4, pp. 657–671, Dec. 2010.



**Wenchao Li** (Member, IEEE) received the B.S. and M.S. degrees in information engineering from the Chengdu University of Technology, Chengdu, China, in 2005 and 2007, respectively, and the Ph.D. degree in electronic engineering from the University of Electronic Science and Technology of China (UESTC), Chengdu, in 2012.

From 2016 to 2017, he was a Visiting Scholar with The Ohio State University, Columbus, OH, USA. He is currently an Associate Research Fellow with the School of Information and Communication Engineering, UESTC. His research interests include radar forward-looking imaging, superresolution, and SAR raw data simulation.



**Lei Wang** received the B.S. degree in communication engineering from Chongqing University, Chongqing, China, in 2022. He is currently working toward the M.S. degree in electronic engineering with the School of Information and Communication Engineering, University of Electronic Science and Technology of China, Chengdu, China, under the supervision of Associate Research Fellow Wenchao Li.

His research interests include SAR raw data simulation and SAR imaging.



**Dan Liu** received the B.S. degree in electronic information science and technology from Chongqing University, Chongqing, China, in 2017, and the M.S. degree in electronic engineering from the University of Electronic Science and Technology of China, Chengdu, China, in 2023.

His research interests include SAR raw data simulation and SAR imaging.



**Tianfu Chen** (Student Member, IEEE) received the B.S. degree in electronic engineering, in 2018, from the University of Electronic Science and Technology of China, Chengdu, China, where he is currently working toward the Ph.D. degree in information and communication engineering.

His research interests include radar signal processing, SAR imaging, and system design.



**Zhongyu Li** (Member, IEEE) received the B.S. and Ph.D. degrees in electronic engineering from the University of Electronic Science and Technology of China (UESTC), Chengdu, China, in 2011, and 2017, respectively.

From 2015 to 2016, he was a Visiting Ph.D. Student with the Department of Information Engineering, Electronics and Telecommunications, Sapienza University of Rome, Rome, Italy. He is currently a Research Fellow with UESTC. His research interests include SAR imaging and ground moving target indication.



**Junjie Wu** (Senior Member, IEEE) received the B.S., M.S., and Ph.D. degrees in electronic engineering from the University of Electronic Science and Technology of China (UESTC), Chengdu, China, in 2004, 2007, and 2013, respectively.

From 2012 to 2013, he was a Visiting Student with the Department of Electrical and Computer Engineering, Duke University, Durham, NC, USA. He is currently a Professor with UESTC. His research interests include bistatic SAR and cognitive radar imaging.



**Haiguang Yang** (Member, IEEE) received the B.S. and Ph.D. degrees in electronic engineering from the University of Electronic Science and Technology of China (UESTC), Chengdu, China, in 2001 and 2013, respectively.

He is currently a Research Fellow with UESTC. His research interests include radar signal processing and SAR imaging.



**Jianyu Yang** (Member, IEEE) received the B.S. degree in electronic engineering from the National University of Defense Technology, Changsha, China, in 1984, and the M.S. and Ph.D. degrees in electronic engineering from the University of Electronic Science and Technology of China (UESTC), Chengdu, China, in 1987 and 1991, respectively.

In 2005, he visited the Massachusetts Institute of Technology, Cambridge, MA, USA. He is currently a Professor with the School of Information and Communication Engineering, UESTC. His research interests include radar imaging, target detection and recognition.